D 2, 463 (1970).

[19] F. Bomse, E. J. Moses, and T. B. Borak, Nuovo Cimento 68A, 383 (1970).

[20] W. J. Kernan, H. B. Crawley, R. A. Jespersen, and R. A. Leacock, Phys. Rev. D 1, 48 (1970).

[21] The OPE vertex form factors used by Colton *et al.* (Ref. 25) differ slightly from those of Wolf, so that the S-wave form factor of Colton *et al.* does not become infinite at threshold. Specifically, Eq. (17e) of Ref. 25 has the term $(M+m_p)$ in both numerator and denominator, while Wolf has $(M \pm m_p)$, where the sign depends on the parity of the πN state.

[22] L. Roper, R. M. Wright, and B. T. Feld, Phys. Rev. 138, B190 (1965).

[23] Particle Data Group, Rev. Mod. Phys. 43, S1 (1971). See p. S114.

[24] Our theoretical t spectrum, Fig. 8(c), disagrees enormously with that of Ref. 3, Fig. 6, which is surprising, since they are analyzing the same reaction at the same laboratory momentum using the same model, OPEW with Benecke-Dürr form factors. Our curve 8(c) fits their data quite well, while their own is a poor fit.

[25] E. Colton, P. E. Schlein, E. Gellert, and G. A. Smith, Phys. Rev. D 3, 1063 (1971).

[26] T. G. Trippe, C.-Y. Chien, E. Malamud, J. Mellema, P. E. Schlein, W. E. Slater, D. H. Stork, and H. K. Ticho, Phys. Letters 28B, 203 (1968).

[27] T. Ferbel, R. Holmes, and S. Stone, Phys. Rev. Letters 22, 1141 (1969).

[28] An exception to this observation is the $p\pi^+$ ($\bar{p}\pi^-$) mass spectrum of Ref. 6, which is in perfect agreement with OPE. However, this agreement results from the fact that the mass of the Δ is a fitted variable in their OPE model. Their fitted value of 1220 MeV is considerably lower than the value 1232 MeV (Ref. 23) used by most authors.

PHYSICAL REVIEW D VOLUME 7, NUMBER 3 1 FEBRUARY 1973

Elastic Scattering and Single-Pion Production in K^+p Reactions at 4.27 GeV/c*

A. Seidl†

The Enrico Fermi Institute and the Department of Physics, University of Chicago, Chicago, Illinois 60637

(Received 12 July 1972)

Elastic K^+p scattering at a beam momentum of 4.27 GeV/c is studied and compared with elastic K^-p scattering in order to extract the imaginary part of the non-Pomeranchukon-exchange amplitude. The single-pion-production cross sections are presented as well as production cross sections and resonance parameters for the $\Delta(1236)$, the $K^{*+}(890)$, and the $K^{*+}(1420)$. Production and decay distributions for the $\Delta^{++}(1236)$ and the $K^{*+}(890)$ are presented and compared with the absorptive particle-exchange model and with Regge-pole-exchange models.

I. INTRODUCTION

The study of states of low multiplicity has yielded much information about the strong interactions.

In this paper we report on elastic scattering and single-pion production as observed in a 7.4-events/μb exposure of the MURA-ANL 30-in. liquid hydrogen bubble chamber to a separated beam of 4.27-GeV/c K^+ mesons. The analysis of similar event topologies at comparable beam momenta can be found in Refs. 1 and 2. Further references can be found in several compilations of K^+-induced reactions.[3,4]

A comparison of K^+p and K^-p elastic scattering yields information on the nondiffractive part of the exchange amplitude.

In the one-pion-production reactions there is copious production of known $K\pi$ and $N\pi$ resonant states. A study of the production and decay properties of these resonant states yields information about the production mechanisms.

In Sec. II of this paper we discuss the collection and reduction of the data. Event selection is discussed in Sec. III. In Sec. IV the elastic scattering data are presented and compared to K^-p elastic scattering at nearby momenta.[5] In Sec. V we present cross sections for the reactions

$$K^+p \to K^+p\pi^0,$$

$$K^+p \to K^0p\pi^+,$$

$$K^+p \to K^+n\pi^+$$

as well as the cross sections for the production of quasi-two-body final states. And, in Sec. VI, we present resonance production and decay distributions and discuss production models for the dominant quasi-two-body final states.

II. THE COLLECTION AND REDUCTION OF THE DATA

The data were collected during two separate exposures of the MURA-ANL liquid-hydrogen bubble chamber to a beam tuned to transport a separated K^+ beam of 4.3 GeV/*c*. The contamination of the beam by light particles, π's and μ's, was measured by a Cherenkov counter just before the bubble chamber. The counting rate of the Cherenkov counter was less than 1% of the total incident flux, a rate consistent with that of a pure K^+ beam with the counts coming from interactions and decays within the counter itself. Even so, no pictures were taken when there was a count in the Cherenkov counter. Thus we believe that the contamination of the beam due to light particles is negligible and no cross-section corrections due to beam π's or μ's have been made.

The beam momentum, design value 4.3 GeV/*c* ± 0.5%, was measured in a number of ways. A set of noninteracting beam tracks were measured and the average momentum, 4.27 ± 0.12 GeV/*c*, was computed. The invariant mass for a set of two- and four-prong events was computed in order to find the center-of-mass energy. This yielded a beam momentum of 4.31 ± 0.14 GeV/*c*. Lastly, the weighted average of the beam momentum was computed for all measured events. The latter procedure was used to determine the stability of the beam momentum over the length of the exposures.

The value of the beam momentum, at the bubble-chamber entrance window, was found to be 4.28 ± 0.02 GeV/*c* for most of the data. Due to a beam magnet change during the second exposure the beam momentum for ~50% of the second exposure was 4.22 ± 0.02 GeV/*c*. The corresponding variation in the center-of-mass energy is 50 MeV and does not effect mass distributions except at the very edge of phase space. Therefore, both sets of data have been combined.

All of the film was double-scanned for all interaction topologies and a conflict scan was made. The scanning efficiency for all but the two-prong events was greater than 99%. The scanning efficiency for the two-prong events is a function of the range of the recoil proton. Reliable corrections can be made when the proton range exceeds 1 cm. These corrections are discussed in Sec. IV.

All events were measured on conventional film plane and image plane digitizers connected directly to an EMR-6050 computer. The computer performed a spatial reconstruction from the track and vertex measurements to ensure that the measurements were accurate. The measurers were required to immediately remeasure any track or vertex which failed the measurement criteria. The measurers were also required to enter an ionization estimate before measuring each track.

Geometric reconstruction was done using NP54 (Ref. 6) and kinematic reconstruction was done using GRIND.[7]

The incident K^+ flux was measured by counting beam tracks in every fiftieth frame within a restricted fiducial volume. The total measured flux is 7.37 ± 0.18 events/μb. Only a fraction of the film was totally analyzed for the two-prong topology. The incident flux for the two-prong topology is 5.30 ± 0.15 events/μb.

III. EVENT SELECTION

The topologies that contribute events to the final states discussed in this paper are the two-prong and the two-prong-plus-V^0 topologies.

From the two-prong topology come the events that fit the reactions

$$K^+p \rightarrow K^+p\,, \tag{1}$$

$$K^+p \rightarrow K^+p\pi^0\,, \tag{2a}$$

$$K^+p \rightarrow K^0p\pi^+\,, \tag{2b}$$

$$K^+p \rightarrow K^+n\pi^+\,. \tag{2c}$$

Reaction (1) has four kinematic constraints and reactions (2a), (2b), and (2c) have only one kinematic constraint, since they have a missing neutral particle.

From the two-prong-plus-V^0 topology, we have events which fit the three-body reaction

$$\begin{aligned} &K^+p \rightarrow K^0p\pi^+\,,\\ &K^0 \rightarrow \pi^+\pi^-\,. \end{aligned} \tag{2b$'$}$$

In these events the neutral K is detected via its $\pi^+\pi^-$ decay mode and they thus have seven kinematic constraints.

The elastic scattering events were divided into three classes. In class *A* we place the events that have a $\chi^2 < 20$ for 4 degrees of freedom and that are consistent with the measurer's ionization estimate

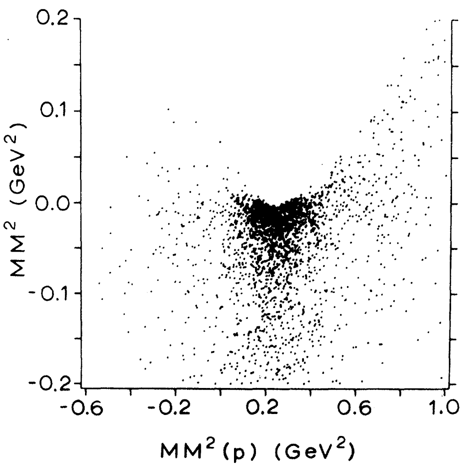

FIG. 1. Scatter plot of MM^2 vs $MM^2(p)$ for class *C* elastic scattering events.

TABLE I. Single-pion production events which are ambiguous between two hypotheses.

Hypothesis with larger χ^2 \ Hypothesis with smaller χ^2	$K^+p\pi^0$	π^+pK^0	π^+K^+n
$pK^+\pi^0$	0	487	133
$p\pi^+K^0$	426	2	46
$K^+\pi^+n$	82	80	1351

(15 333 events).[8] In class *B* we place the events with a $\chi^2 < 20$ for 4 degrees of freedom, but inconsistent with the measurer's ionization estimate (2453 events). A rescan of a sample of class *B* events showed that under closer examination the elastic hypothesis was preferred. In class *C* we place the events with $\chi^2 > 20$ for the elastic hypothesis.

In order to extract the elastic sample from the class *C* events, we have imposed missing-mass-squared cuts, $-0.06 \leq \mathrm{MM}^2 \leq 0.02\ \mathrm{GeV}^2$, and cuts on the unfitted mass squared recoiling against the proton, $0.0 \leq M^2 < 0.4\ \mathrm{GeV}^2$. In Fig. 1 we show a scatter plot of the missing mass squared versus the mass squared recoiling against the proton for the class *C* events. A clear elastic signal is evident (1479 events).

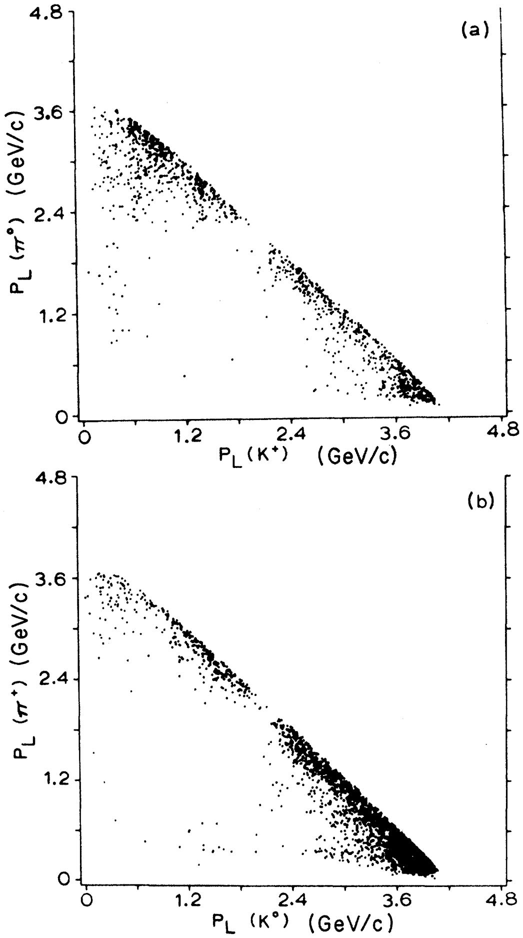

FIG. 2. Scatter plot of the laboratory momentum of the *K* vs the laboratory momentum of the π for: (a) the unambiguous events of hypothesis (2a); (b) the unambiguous events of hypothesis (2b).

The best sample of events in which a neutral particle is produced is that of reaction (2b′) where the neutral particle is detected via a charged decay mode. A two-prong-plus-V^0 event was accepted as belonging to the $K^0p\pi^+$ final state whenever it made both a four-constraint production fit ($\chi^2 < 20$) and a seven-constraint double-vertex fit ($\chi^2 < 35$) with all tracks having ionization consis-

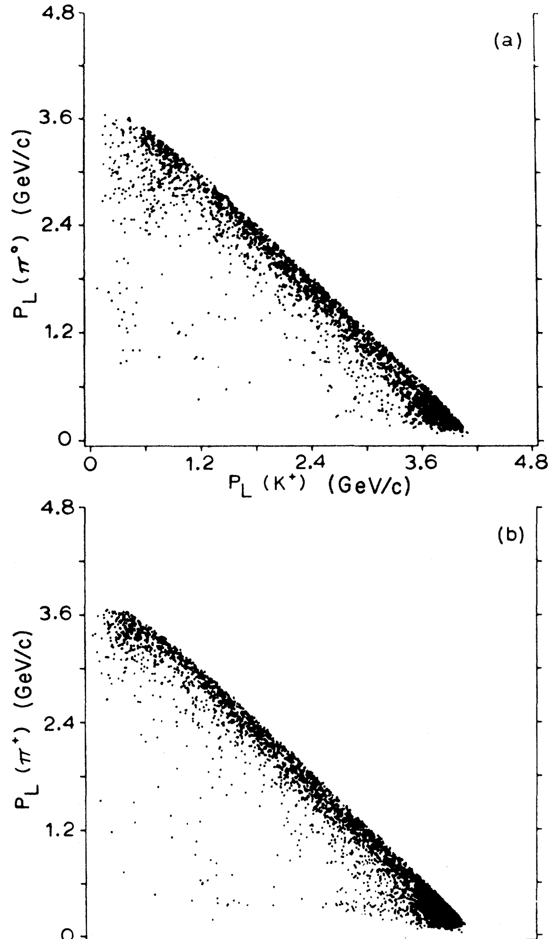

FIG. 3. Scatter plot of the laboratory momentum of the *K* vs the laboratory momentum of the π for: (a) the unambiguous and selected ambiguous events of hypothesis (2a); (b) the unambiguous and selected ambiguous events of hypothesis (2b).

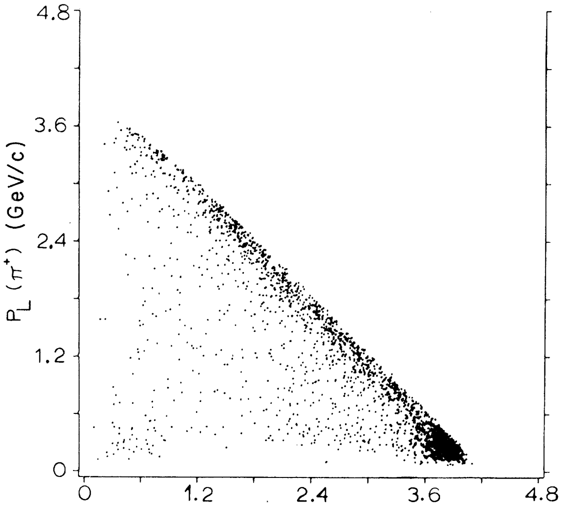

FIG. 4. Scatter plot of the laboratory momentum of the K vs the laboratory momentum of the π for the events with a visible K^0 decay.

tent with the mass assignment and the fitted momenta (1935 events). These events are highly overconstrained and are thus free from multineutral background. Since the K^0 is identified by its decay, there is no problem of $K\pi$ ambiguity.

The two-prong events with a missing neutral have only one kinematic constraint and are thus more difficult to identify correctly than the more highly constrained events. We have accepted all hypotheses with $\chi^2 < 6$ and consistent with the observed ionization. This yielded an unambiguous choice for 1850, 3238, and 2485 events of reactions (2a), (2b), and (2c), respectively.

The number of twofold ambiguous events is shown in Table I. The row index is for the hypothesis with the smaller χ^2, the column index is for the hypothesis with the larger χ^2. In addition, there are 119 events ambiguous between three or more hypotheses. The ambiguous events tend to fall in the region of phase space where the laboratory momenta of both mesons is ~2 GeV/c. For mesons of this momentum there is essentially no kinematic difference caused by a $K\pi$ mass interchange. Both tracks are minimum-ionizing so that ionization criteria do not remove the ambiguity.

Several methods of resolving the ambiguity were attempted. The simplest method, and one that works at least as well as any other, is choosing the hypothesis with the lower χ^2. To show that this is not an unreasonable choice, we present in Fig. 2 a scatter plot of the laboratory momentum of the π versus the laboratory momentum of the K for the unambiguous events of reactions (2a) and (2b). A clear depletion of events can be seen where the momenta of the two mesons are large and approximately equal. In Fig. 3 we show the momentum scatter plots with the ambiguous events chosen by the χ^2 criterion included. The dips in the momentum distributions are now filled in the correct proportion. For comparison, we show in Fig. 4 a similar plot for the events of reaction (2b′) where there are no $K\pi$ ambiguities. The similarity of this distribution, Fig. 4, to that of Fig. 3(b) convinces us that we have resolved the ambiguity correctly in the majority of the cases.[9]

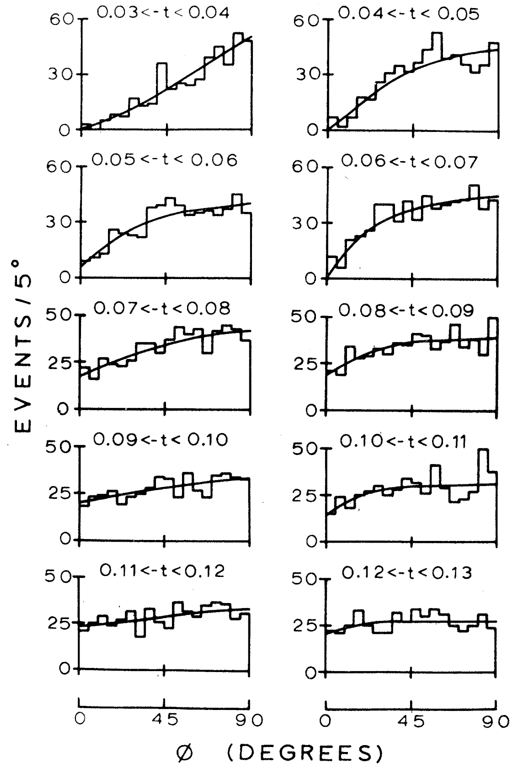

FIG. 5. Distributions of the angle ϕ for elastic events for various choices of momentum transfer. The curves are the fits to the form $dN/d\phi = A - B\cos\phi\,\exp(-C\sin\phi)$. The units of t are GeV^2.

In addition, since the one-constraint events have background from events with multineutrals, we have imposed missing-mass-squared cuts of $-0.07 \leq MM^2 \leq 0.10$ GeV^2, $0.15 \leq MM^2 \leq 0.35$ GeV^2, and $0.68 \leq MM^2 \leq 1.08$ GeV^2 for the events of reactions (2a), (2b), and (2c), respectively.

IV. ELASTIC SCATTERING

In order to study elastic scattering at low momentum transfer, corrections must be made for event losses. Events are lost whenever the proton has insufficient projected length to be readily visible on the scanning table. These losses are illus-

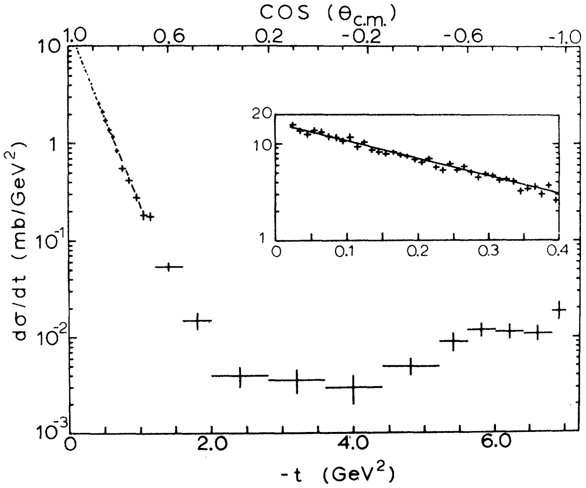

FIG. 6. Differential cross section $d\sigma/dt$ for elastic scattering. The curve is the fit to the form $d\sigma/dt = A\exp(Bt)$ in the $-t$ range 0.03 to 1.0 GeV^2.

trated by plotting the angle ϕ defined by

$$\cos\phi = (\hat{k}_{\text{in}} \times \hat{k}_{\text{out}} / |\hat{k}_{\text{in}} \times \hat{k}_{\text{out}}|) \cdot (\hat{z} \times \hat{k}_{\text{in}} / |\hat{z} \times \hat{k}_{\text{in}}|),$$

where $\hat{k}_{\text{in}}$ is the unit vector in the incoming K^+ direction, $\hat{k}_{\text{out}}$ is the unit vector in the outgoing K^+ direction, and $\hat{z}$ is the unit vector normal to the bubble-chamber camera plane. We plot ϕ for various choices of momentum transfer in Fig. 5.

The angle ϕ is the azimuthal angle of the outgoing proton about the incoming K^+ direction. If the target proton is unpolarized, ϕ should be isotropically distributed. There is, however, a depletion of events at small ϕ in the experimental distributions. This depletion becomes more and more severe as t, the four-momentum transfer squared, decreases. A value of $\phi = 0$ implies that the proton is going directly towards or away from the bubble-chamber cameras. In this case the proton has zero projected length and it is clear that these events will be missed.

In order to correct for these azimuthal losses we have fit each of the ϕ distributions to the phenomenological form

$$\frac{dN}{d\phi} = A - B\cos\phi\exp(-C\sin\phi).$$

The parameters A, B, and C were determined by minimizing the χ^2 for the fit (typical probability of 37%). The parameter A is the corrected number of events in each interval of t. The curves in Fig. 5 are the results of the fit.

The differential cross section, $d\sigma/dt$, is shown in Fig. 6 and Table II. We have fitted the differen-

TABLE II. Elastic differential cross section.

$-t$ range (GeV^2)	Events [a]	$d\sigma/dt$ (mb/GeV^2)	$-t$ range (GeV^2)	Events	$d\sigma/dt$ (mb/GeV^2)
0.03–0.04	818 ± 63	15.44 ± 1.22	0.29–0.30	238	4.49 ± 0.30
0.04–0.05	731 ± 47	13.79 ± 0.93	0.30–0.31	259	4.89 ± 0.32
0.05–0.06	653 ± 45	12.30 ± 0.89	0.31–0.32	247	4.66 ± 0.31
0.06–0.07	732 ± 46	13.81 ± 0.91	0.32–0.33	224	4.23 ± 0.29
0.07–0.08	697 ± 55	13.16 ± 1.06	0.33–0.34	229	4.32 ± 0.30
0.08–0.09	631 ± 45	11.90 ± 0.89	0.34–0.35	216	4.08 ± 0.29
0.09–0.10	601 ± 62	11.34 ± 1.19	0.35–0.36	176	3.21 ± 0.26
0.10–0.11	553 ± 40	10.43 ± 0.78	0.36–0.37	181	3.42 ± 0.26
0.11–0.12	606 ± 61	11.43 ± 1.17	0.37–0.38	193	3.64 ± 0.27
0.12–0.13	491 ± 33	9.26 ± 0.65	0.38–0.39	159	3.00 ± 0.25
0.13–0.14	544 ± 30	10.26 ± 0.60	0.39–0.40	197	3.72 ± 0.27
0.14–0.15	464 ± 27	8.75 ± 0.54	0.40–0.425	345	2.60 ± 0.15
0.15–0.16	430	8.11 ± 0.42	0.425–0.45	353	2.66 ± 0.15
0.16–0.17	417	7.87 ± 0.41	0.45–0.475	306	2.31 ± 0.14
0.17–0.18	434	8.19 ± 0.42	0.475–0.50	289	2.18 ± 0.14
0.18–0.19	407	7.68 ± 0.41	0.50–0.525	247	1.86 ± 0.12
0.19–0.20	397	7.49 ± 0.40	0.525–0.55	222	1.68 ± 0.12
0.20–0.21	364	6.87 ± 0.38	0.55–0.575	187	1.41 ± 0.11
0.21–0.22	339	6.40 ± 0.37	0.575–0.60	185	1.40 ± 0.11
0.22–0.23	372	7.02 ± 0.39	0.60–0.625	167	1.26 ± 0.10
0.23–0.24	304	5.74 ± 0.35	0.625–0.65	145	1.09 ± 0.09
0.24–0.25	280	5.28 ± 0.33	0.65–0.675	120	0.91 ± 0.08
0.25–0.26	327	6.17 ± 0.36	0.675–0.70	109	0.82 ± 0.08
0.26–0.27	279	5.26 ± 0.33	0.7–0.8	350	0.66 ± 0.04
0.27–0.28	309	5.83 ± 0.35	0.8–0.9	222	0.42 ± 0.03
0.28–0.29	270	5.09 ± 0.33	0.9–1.0	149	0.28 ± 0.02

[a] Events with quoted errors corrected for azimuthal losses.

tial cross section in the range $0.03 \leq -t \leq 1.0$ GeV^2 to the forms

$$\frac{d\sigma}{dt} = A \exp Bt$$

and

$$\frac{d\sigma}{dt} = A \exp(Bt + Ct^2).$$

In Table III we show the best-fit parameters and we plot in Fig. 6 the results of the linear exponential fit. The elastic cross section, corrected for azimuthal losses, is 4.128 ± 0.122 mb.

Using the extrapolated value of $d\sigma/dt$ at $t=0$ for the elastic events and the total K^+p cross section, we can determine the modulus of the ratio of the real to the imaginary part of the elastic K^+p scattering amplitude at $t=0$. The optical theorem relates the total cross section to the imaginary part of the forward elastic scattering amplitude

$$\text{Im} f_{\text{el}}(0) = \sigma_T/\hbar c(16\pi)^{1/2}.$$

The forward differential cross section is given by

$$\left.\frac{d\sigma}{dt}\right|_{t=0} = [\text{Im} f_{\text{el}}(0)]^2 + [\text{Re} f_{\text{el}}(0)]^2 .$$

Combining these equations we have

$$\left.\frac{d\sigma}{dt}\right|_{t=0} = \frac{\sigma_T{}^2(1+\alpha^2)}{16\pi(\hbar c)^2},$$

where

$$\alpha^2 = |\text{Re} f_{\text{el}}(0)/\text{Im} f_{\text{el}}(0)|^2 .$$

Using the linear exponential extrapolation for the forward differential cross section and an interpolated value of the total K^+p cross section at 4.27 GeV/c of 17.3 ± 0.1 mb,[3] we find that[10]

$$\alpha^2 = 0.120 \pm 0.036 .$$

The large value of the real part of the elastic scattering amplitude (Ref = 35% Imf) indicates that other trajectories, in addition to that of the Pomeranchuk trajectory which is pure imaginary, contribute to K^+p elastic scattering in the forward direction.

Figure 6 also shows that the elastic differential cross section has a peak in the backward direction. This backward peak is indicative of Y^* exchange in the u channel, u being the crossed four-momentum transfer squared. The cross section in the backward direction ($-1.0 < \cos\theta_{\text{c.m.}} < -0.9$) is equal to 7.9 ± 1.2 μb.

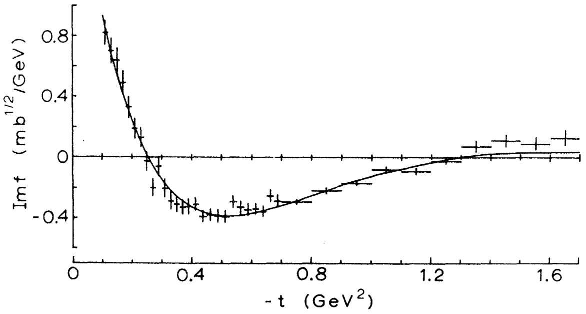

FIG. 7. Plot of $\frac{d\sigma/dt\,(K^-p) - d\sigma/dt\,(K^+p)}{2[d\sigma/dt\,(K^+p)]^{1/2}}$. The K^-p data have been taken from Ref. 1 – averaging the data at 3.9 and 4.6 GeV/c. The curve is the fit to the form $A \exp(Bt)\, J_0(C\sqrt{-t})$.

Davier and Harari[11] have recently pointed out that by making certain assumptions a comparison of K^+p and K^-p elastic scattering yield information on the imaginary part of the nondiffractive nonflip elastic scattering amplitude. The assumptions are: (a) The dominant diffractive amplitude is pure imaginary and contributes only to the spin-nonflip amplitude; (b) one can neglect the square of the nondiffractive nonflip amplitude compared to the diffractive amplitude squared and to the interference term between these two amplitudes; and (c) the nondiffractive nonflip amplitude in K^+p scattering is purely real since there are no s-channel K^+p resonances. With these assumptions

$$\text{Im} f_{\Delta\lambda=0} = \frac{d\sigma/dt(K^-p) - d\sigma/dt(K^+p)}{2[\,d\sigma/dt(K^+p)]^{1/2}},$$

where $f_{\Delta\lambda=0}$ is the nondiffractive nonflip amplitude.

In Fig. 7 we plot Im$f_{\Delta\lambda=0}$ as a function of t. We have used the elastic scattering data of Ref. 5, averaging the data at beam momenta of 3.9 GeV/c and 4.6 GeV/c. The data are fitted to the form

$$\text{Im} f_{\Delta\lambda=0} = A \exp(Bt) J_0(C\sqrt{-t}).$$

TABLE III. Parameters for the forward elastic differential cross section.

Form fitted	χ^2/NDF [a]	A (mb/GeV^2)	B (GeV^{-2})	C (GeV^{-4})
$A \exp(Bt)$	46.7/50	17.12 ± 0.52	4.33 ± 0.05	···
$A \exp(Bt + Ct^2)$	45.5/49	16.77 ± 0.52	4.23 ± 0.05	−0.11 ± 0.08

[a] Number of degrees of freedom.

TABLE IV. Reaction cross sections.

Reaction	Number of events[a]	Cross section (mb)
$K^+p \rightarrow K^+p$	$21\,880 \pm 239$	4.128 ± 0.122
$K^+p \rightarrow K^+p\pi^0$	2141 ± 123	0.404 ± 0.026
$K^+p \rightarrow K^0p\pi^+$ (K^0 not detected)	4308 ± 170	1.078 ± 0.052[b]
$K^+p \rightarrow K^0p\pi^+$ ($K^0 \rightarrow \pi^+\pi$)	1935 ± 44	1.069 ± 0.037[c]
$K^+p \rightarrow K^+n\pi^+$	3600 ± 154	0.679 ± 0.034

[a] Number of events for reactions with a missing neutral estimated from missing-mass-squared distributions. Number of elastic events corrected for azimuthal losses.

[b] Cross section corrected for not using visible K^0 decays.

[c] Cross section corrected for unseen K^0 decays.

We have made the small-angle approximation

$$P_l(\cos\theta) = J_0(\sqrt{-t}\,(l+\tfrac{1}{2})/q), \quad q = \text{c.m. momentum}.$$

The fitted results are $A = 2.2 \pm 0.1$ mb$^{1/2}$/GeV, $B = 1.4 \pm 0.1$ GeV^{-2}, and $C = 4.8 \pm 0.1$ GeV$^{-1} = 0.95 \pm 0.02$ F. The value of C corresponds to a dominant partial wave of $J \simeq \frac{13}{2}$ and indicates that the imaginary part of the non-Pomeranchukon-exchange amplitude is itself peripheral.

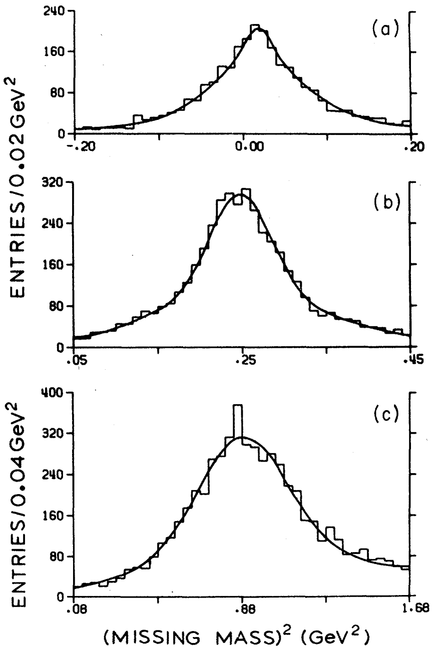

FIG. 8. Missing-mass-squared distributions in which each event has been weighted inversely by the number of acceptable fits made for: (a) hypothesis (2a); (b) hypothesis (2b); (c) hypothesis (2c). The curves are fits to a superposition of Gaussians and a polynomial background.

Our determination of the parameters B and C is in good agreement with the values determined in Ref. 8 at a beam momentum of 5 GeV/c. The parameter A, which is approximately proportional to the difference in the squares of the K^-p and the K^+p total cross sections, reflects the change in the K^-p total cross section which drops slightly (1 ± 1 mb) in the beam-momentum range of 4.27–5 GeV/c.

V. REACTION CROSS SECTIONS

The cross section for the $K^0p\pi^+$ final state can be measured using only the events with an observed K^0 decay. We compute the probability, for each event, of observing the K^0 decay in the bubble chamber. The weight assigned to each event is then the inverse of the detection probability. The cross section, determined by the flux and the sum of the weights, is given in Table IV. The cross section for reactions (2a), (2b), and (2c) are also collected in Table IV.

The determination of the cross sections for the reactions with a missing neutral is not as straightforward since these reactions have a non-negligible background present. We plot in Fig. 8 the missing mass squared for the events selected, using the criteria of Sec. III with the exception of the missing-mass-squared criterion. Whenever an event made more than one acceptable fit, that entry was weighted by the inverse of the number of acceptable fits made.

In each of the missing-mass-squared distributions a signal centered at the mass of the missing neutral can be seen. In order to extract the number of events in the signal, we have fitted each of the

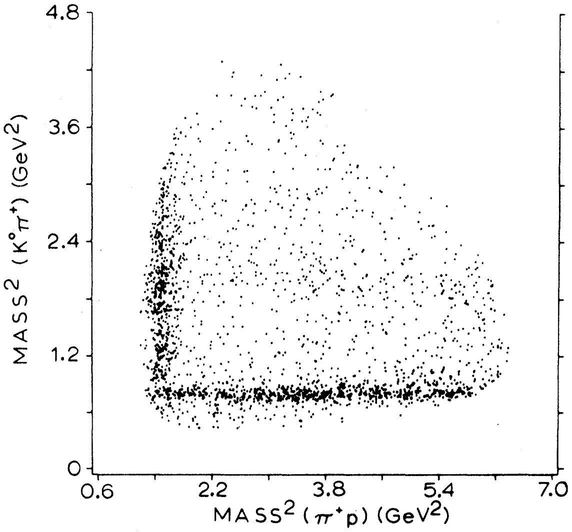

FIG. 9. Dalitz plot for the events with a visible K^0 decay.

missing-mass-squared distributions to the form

$$\frac{dN}{d m_{\mathrm{MM}}^2} = A_1 \exp\left(\frac{-(m_{\mathrm{MM}}^2 - M_0^2)^2}{2\sigma_1^2}\right) + A_2 \exp\left(\frac{-(m_{\mathrm{MM}}^2 - M_0^2)^2}{2\sigma_2^2}\right) + B_0 + B_1 m_{\mathrm{MM}}^2 + B_2 m_{\mathrm{MM}}^4 + \cdots ,$$

where m_{MM}^2 is the missing mass squared, M_0^2 is the π^0, K^0, or n mass squared, and A_1, A_2, σ_1, σ_2, B_0, B_1, and B_2 are parameters to be determined by the fit.

In order to achieve fits with acceptable χ^2, both Gaussians and a quadratic background polynomial were needed. The Gaussians, chosen since they reflect the expected distribution of the measurement errors, represent the contribution of the signal. The number of events in the signal is given by

$$N = (2\pi)^{1/2}(A_1\sigma_1 + A_2\sigma_2) .$$

In Fig. 9 we show the Dalitz plot for the events of reaction (2b′), the $K^0 p \pi^+$ final state with a visible K^0 decay. Prominent resonance bands for the $K^{*+}(890)$, the $\Delta^{++}(1236)$, and a fainter resonance band for the $K^{*+}(1420)$ are clearly visible.

Since these events have seven kinematic constraints, they are free from any multineutral background contamination. We have done a detailed Dalitz-plot analysis in order to extract the resonance fractions as well as the other resonance parameters. The analysis was a maximum-likelihood fit, using weighted events, with a probability function of

$$\frac{dN}{dM_{K\pi}^2 dM_{p\pi}^2} = f_{ps} + f_{K^*(890)} B^2(K^*(890)) W(K^*(890)) + f_{K^*(1420)} B^2(K^*(1420)) + f_{\Delta(1236)} B^2(\Delta(1236)) W(\Delta(1236)) ,$$

where f_i is the fraction associated with phase space or resonance production, $B^2(i)$ is the appropriate Breit-Wigner form, and $W(i)$ is the angular distribution of the resonance decay products in the helicity frame.

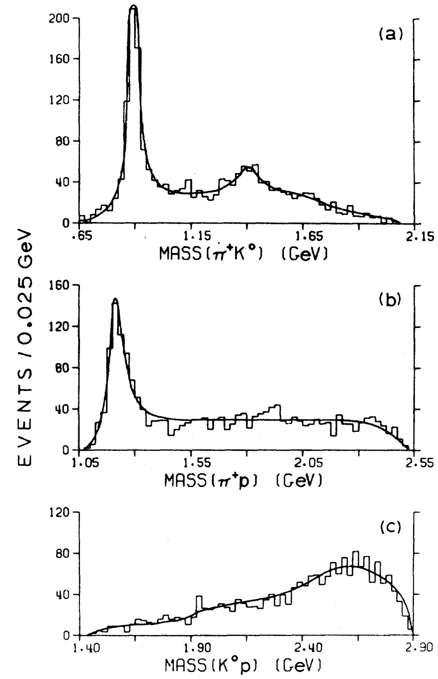

FIG. 10. Mass projections for events with a visible K^0 decay: (a) mass(π^+K^0), (b) mass(π^+p), and (c) mass(K^0p). The curves are the results of a Dalitz-plot fit.

Due to the relatively small number of events in the $K^*(1420)$ band, we are not sensitive, in this fit, to the $K^*(1420)$ decay distribution. We therefore assumed it to be constant.

The best-fit parameters are presented in Table V. The cross sections are corrected for the unseen K^0 decay modes. In Fig. 10 we plot the three mass projections with the results of the fit superimposed.

The events with a missing neutral, reactions (2a), (2b), and (2c), are contaminated by some background as can be seen in the missing-mass-squared plots of Fig. 8. In addition, as discussed in Sec. III, a sizable fraction of these events have

TABLE V. Resonance parameters determined from Dalitz-plot analysis of visible K^0 events.

Resonance	Mass (MeV)	Width (MeV)	Fraction (%)	Cross section[a] (μb)
$\Delta^{++}(1236) \to \pi^+ p$	1223.6 ± 1.6	91.6 ± 6.1	33.69 ± 1.68	360 ± 20
$K^{*+}(890) \to \pi^+ K^0$	894.2 ± 1.1	58.8 ± 2.8	39.45 ± 1.88	422 ± 22
$K^{*+}(1420) \to \pi^+ K^0$	1409.4 ± 5.9	99.3 ± 15.0	7.98 ± 0.82	85 ± 9
Nonresonant	···	···	18.88 ± 1.36	202 ± 15

[a] Cross sections corrected for unseen K^0 decays.

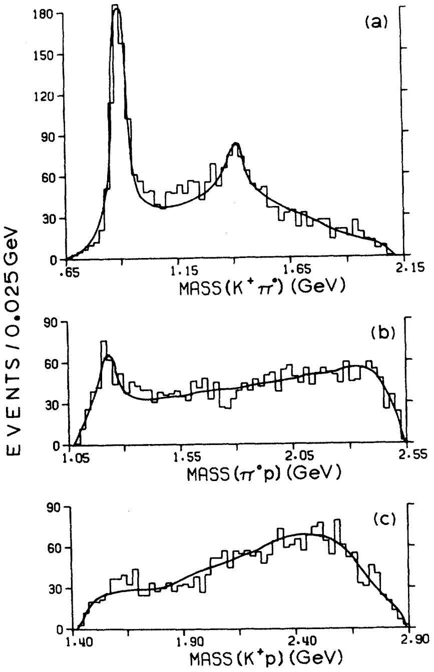

FIG. 11. Mass projections for events with a missing π^0: (a) mass($\pi^0 K^+$), (b) mass($\pi^0 p$), and (c) mass(K^+p). The curves are fits to Breit-Wigner(s) and a polynomial background taking into account reflections due to resonances in other two-body mass combinations.

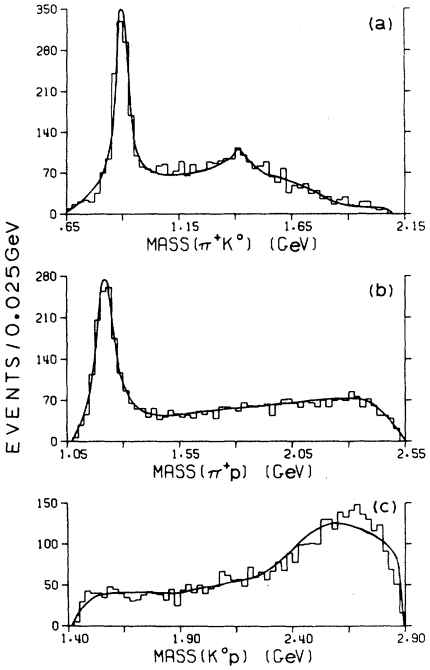

FIG. 12. Mass projections for the events with a missing K^0: (a) mass(π^+K^0), (b) mass(π^+p), and (c) mass (K^0p). The curves result from similar fits as in Fig. 11.

$K\pi$ ambiguities. For these reasons, we have not made as detailed a fit in order to extract the resonance parameters.

In Figs. 11 and 12 we present the mass plots for the events of reactions (2a) and (2b), respectively. The $K^{*+}(890)$ and the $K^{*+}(1420)$ are evident in the $(K\pi)^+$ mass plots, and the $\Delta^{++}(1236)$ is evident in the π^+p mass plot. We have fitted these mass spectra with a superposition of Breit-Wigner forms and a polynomial background term. The curves in Figs. 11 and 12 are a result of the fits and the resonance parameters, determined from the events with a missing neutral, and are collected in Table VI.

VI. RESONANCE PRODUCTION AND DECAY

When one of the particles in the final state is a resonance, information about the production process can be obtained not only from the production angular distribution, but also from the angular distribution of the resonance decay products. For peripheral processes, a convenient, but by no

TABLE VI. Resonance parameters determined from analysis of events with a missing neutral.

Resonance	Mass (MeV)	Width (MeV)	Events [a]	Cross section (μb)
$\Delta^+(1236)\to p\pi^0$	1219.9 ± 5.9	100.0 (input)	276 ± 32	52 ± 6
$K^{*+}(890)\to K^+\pi^0$	896.7 ± 2.1	64.1 ± 4.2	917 ± 80	173 ± 15
$K^{*+}(1420)\to K^+\pi^0$	1407.1 ± 8.5	100.0 (input)	249 ± 26	47 ± 5
$\Delta^{++}(1236)\to p\pi^+$	1216.6 ± 2.1	89.4 ± 4.3	1574 ± 100	395 ± 25 [b]
$K^{*+}(890)\to K^0\pi^+$	893.6 ± 1.6	61.2 ± 3.2	1474 ± 120	370 ± 30 [b]
$K^{*+}(1420)\to K^0\pi^+$	1411.8 ± 9.8	100.0 (input)	299 ± 40	75 ± 10 [b]

[a] Corrected for events eliminated by missing-mass-squared criterion.

[b] Cross section corrected for not using visible K^0 decays.

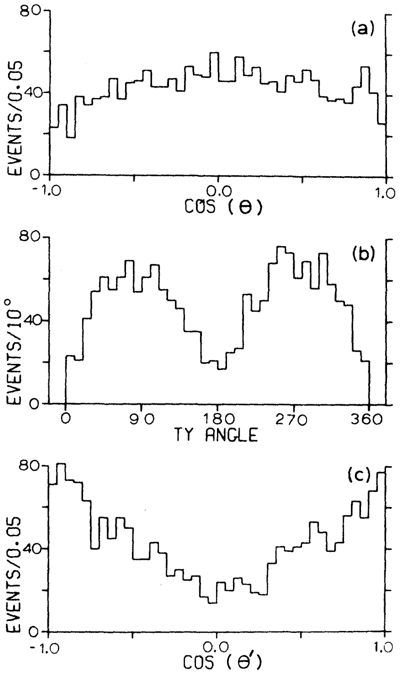

FIG. 13. Decay distributions in the $\Delta^{++}(1236)$ rest frame: (a) cosine of the p-p scattering angle, (b) Treiman-Yang angle, and (c) cosine of the angle between the final-state proton and the production-plane normal.

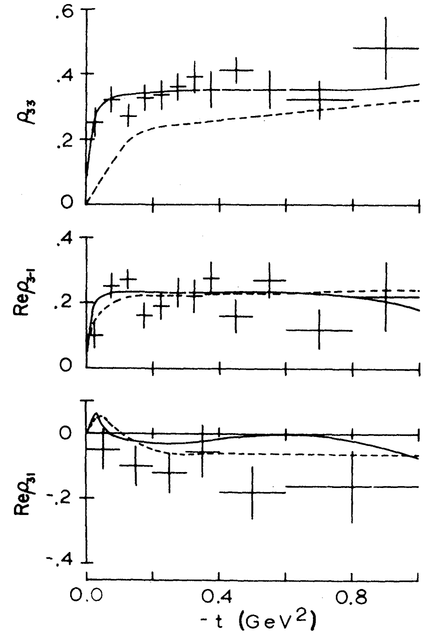

FIG. 14. Density-matrix elements in the Gottfried-Jackson frame as a function of t for the $\Delta^{++}(1236)$ events. The solid curve is the Regge-model prediction of Ref. 12 and the dashed curve is the absorptive-model prediction.

means necessary, choice of coordinate systems in which to study the decay angular distributions is one that emphasizes the exchange particle. This coordinate system, the Gottfried-Jackson frame,[12] is defined in the rest system of the decaying resonance and has its quantization direction parallel to the direction of the momentum of the exchange particle. With the proper choice of y axis, the azimuthal angle is the well-known Treiman-Yang angle.

Another commonly used coordinate system is the helicity frame. The helicity frame emphasizes the produced resonance rather than the exchange particle. The quantization axis in this frame is antiparallel to the line of flight of the particle recoiling against the produced resonance as seen from the resonance rest frame.

In either coordinate frame, the spin population of a resonance can be described by a Hermitian density matrix $\rho_{mm'}$, where m and m' are the magnetic quantum numbers relative to the quantization axis.

TABLE VII. Density-matrix elements for the $\Delta^{++}(1236)$.

$-t$ range (GeV^2)	Events	Gottfried-Jackson frame ρ_{33}	$\rho_{3\,-1}$	$\mathrm{Re}\rho_{31}$	Helicity frame ρ_{33}	$\rho_{3\,-1}$	$\mathrm{Re}\rho_{31}$
0.00–0.05	159	0.251 ± 0.044	0.100 ± 0.042	0.071 ± 0.093	0.254 ± 0.046	0.078 ± 0.044	0.176 ± 0.093
0.05–0.10	198	0.318 ± 0.039	0.250 ± 0.038	−0.149 ± 0.074	0.425 ± 0.034	0.189 ± 0.043	−0.049 ± 0.083
0.10–0.15	253	0.271 ± 0.035	0.269 ± 0.032	−0.011 ± 0.063	0.416 ± 0.030	0.184 ± 0.037	0.088 ± 0.074
0.15–0.20	190	0.325 ± 0.037	0.162 ± 0.038	−0.225 ± 0.082	0.322 ± 0.037	0.163 ± 0.040	0.202 ± 0.081
0.20–0.25	163	0.334 ± 0.043	0.188 ± 0.042	−0.151 ± 0.087	0.370 ± 0.040	0.167 ± 0.046	−0.141 ± 0.091
0.25–0.30	159	0.360 ± 0.038	0.227 ± 0.044	−0.093 ± 0.087	0.377 ± 0.039	0.218 ± 0.044	0.024 ± 0.089
0.30–0.35	105	0.389 ± 0.052	0.223 ± 0.052	−0.053 ± 0.110	0.352 ± 0.049	0.244 ± 0.053	0.051 ± 0.106
0.35–0.40	86	0.347 ± 0.055	0.275 ± 0.052	−0.059 ± 0.113	0.434 ± 0.048	0.225 ± 0.061	−0.065 ± 0.124
0.40–0.50	137	0.410 ± 0.039	0.161 ± 0.047	−0.175 ± 0.101	0.312 ± 0.043	0.218 ± 0.044	0.055 ± 0.093
0.50–0.60	73	0.353 ± 0.059	0.271 ± 0.057	−0.191 ± 0.122	0.418 ± 0.050	0.233 ± 0.065	−0.165 ± 0.131
0.60–0.80	79	0.323 ± 0.063	0.123 ± 0.061	−0.173 ± 0.132	0.337 ± 0.058	0.114 ± 0.068	0.103 ± 0.135
0.80–1.00	27	0.479 ± 0.094	0.221 ± 0.105	−0.184 ± 0.227	0.306 ± 0.098	0.321 ± 0.098	−0.161 ± 0.187
All t	1725	0.328 ± 0.013	0.204 ± 0.013	−0.090 ± 0.027	0.366 ± 0.012	0.182 ± 0.014	0.028 ± 0.028

A. The $\Delta^{++}(1236)K^0$ Final State

For a study of the $\Delta^{++}(1236)K^0$ final state, reaction (3), we have combined the data from reactions (2b) and (2b′). The $\Delta^{++}(1236)$ is defined as a π^+p mass combination in the interval $1.13 < M_{p\pi} < 1.31$ GeV. Since the background level in this mass region is small (<10%), we have not attempted any background subtraction.

The normalized decay distribution is given by

$$W(\theta, \phi) = \frac{3}{4\pi}\Big[\tfrac{1}{6}(1+4\rho_{33}) + \tfrac{1}{2}(1-4\rho_{33})\cos^2\theta + (2/\sqrt{3})\,\mathrm{Re}\rho_{3\,-1}\sin^2\theta\cos 2\phi - (2/\sqrt{3})\,\mathrm{Re}\rho_{31}\sin 2\theta\cos\phi\Big],$$

where, for simplicity, we have written the density-matrix elements as $\rho_{2m2m'}$. In Figs. 13(a) and 13(b) we show the $\cos\theta$ distribution and the ϕ distribution integrated over all other variables. The $\sin^2\theta$ dependence of the scattering angle and the $\sin^2\phi$ dependence of the Treiman-Yang angle are indicative of vector-meson exchange.

A simple model for $\Delta(1236)$ production has been proposed by Stodolsky and Sakurai.[13] Noting that the ρ meson has the same quantum numbers as the γ (photon) the authors have treated the $p\rho\Delta$ vertex in analogy to the $p\gamma\Delta$ vertex. The latter vertex occurs in the photoproduction of a pion. For the magnetic dipole transition $M1$, which dominates pion photoproduction, the angular distribution has a simple form in the coordinate system which has the z axis along the production plane normal:

$$W(\theta', \phi') = \frac{1}{8\pi}(1+3\cos^2\theta').$$

In terms of the Gottfried-Jackson angles

$$\cos^2\theta' = \sin^2\theta\sin^2\phi.$$

The distribution of $\cos\theta'$ is given in Fig. 13(c). When this distribution is fitted to a second-order polynomial in $\cos\theta'$, we find that

$$W(\theta') \sim [1 - (0.15 \pm 0.08)\cos\theta' + (2.3 \pm 0.1)\cos^2\theta'].$$

The departure of the coefficient of the $\cos^2\theta$ term from the Stodolsky-Sakurai value of 3.0 indicates the presence of absorption or other exchange processes.

In Fig. 14 we plot the $\Delta^{++}(1236)$ density-matrix elements evaluated in the Gottfried-Jackson frame. The Gottfried-Jackson density-matrix elements, as well as the helicity density-matrix elements, are tabulated in Table VII. The density-matrix elements as a function of t provide a more sensitive test of the production model. The data are in good agreement with the Stodolsky-Sakurai prediction of

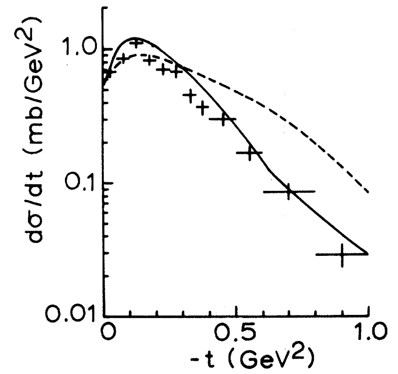

FIG. 15. Differential cross section $d\sigma/dt$ for the $\Delta^{++}(1236)$. The curves result from the same models as in Fig. 14.

$$\rho_{33} = 0.375, \quad \mathrm{Re}\rho_{3\,-1} = 0.216, \quad \mathrm{Re}\rho_{31} = 0.$$

However, the simple model totally fails to account for the scale and the shape of the production distribution, $d\sigma/dt$, plotted in Fig. 15 and tabulated in Table VIII. In fact, even when absorption in the initial and final states is taken into account,[14] the dashed curves in Figs. 14 and 15, the ρ-exchange model fails to account for the production distribution.

In our calculation of the absorptive model, we have used the formulation of Ref. 14 with the parameters

$$\gamma_1 = 0.0707, \quad C_1 = 0.873, \quad \gamma_f = 0.056, \quad C_f = 1.0,$$

and the coupling constants of

$$(f_{K\rho K}G'_{p\rho\Delta}/4\pi)^2 = 42.$$

Regge-exchange models have had considerable success in fitting production distributions. We have explicitly calculated the Regge model of

TABLE VIII. Differential cross section for the reaction $K^+p \rightarrow \Delta^{++}(1236)K^0$.

$-t$ range (GeV^2)	Events	Cross section (μb/GeV^2)
0.00–0.05	159	689 ± 64
0.05–0.10	198	859 ± 74
0.10–0.15	253	1097 ± 88
0.15–0.20	190	824 ± 72
0.20–0.25	163	707 ± 65
0.25–0.30	159	689 ± 64
0.30–0.35	105	455 ± 50
0.35–0.40	86	373 ± 44
0.4–0.5	137	297 ± 29
0.5–0.6	73	158 ± 20
0.6–0.8	79	86 ± 11
0.8–1.0	27	29 ± 6
1.0–1.5	21	9 ± 2

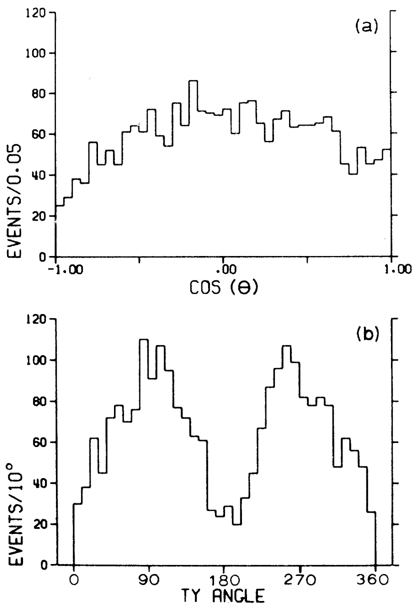

FIG. 16. Decay distributions in the K^{*+}(890) rest frame: (a) cosine of the K-K scattering angle, (b) Treiman-Yang angle.

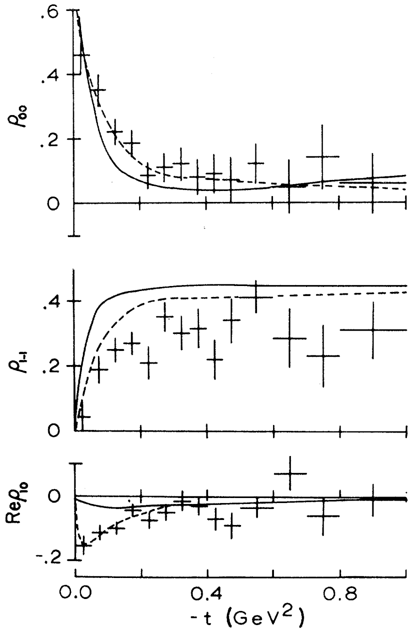

FIG. 17. Density-matrix elements in the Gottfried-Jackson frame as a function of t for the K^{*+}(890). The solid curves are the predictions of the Regge model of Ref. 15 and the dashed curve is the absorptive-model prediction.

Krammer and Maor[15] for reaction (3). The results of this calculation are shown as the solid curves in Figs. 14 and 15. The model is in reasonable agreement with the data from this experiment, both in the shapes of the distributions and in the over-all normalization.

The Krammer and Maor model involves the exchange of the ρ and the A_2 trajectories. In order to reduce the number of free parameters, the authors have used the ρ trajectory as determined by the reaction $\pi^- p \to \pi^0 n$ and the A_2 trajectory as determined by the reaction $\pi^- p \to \eta n$. Using SU_3 symmetry, the authors have related the ρ-exchange residue functions for reaction (3) to those determined from the reaction $\pi^+ p \to \pi^0 \Delta^{++}(1236)$. The remaining parameters, six in all, related to the A_2-exchange residue functions for reaction (3), were determined by fits to the existing data on reaction (3) in the beam-momentum range 3-5 GeV/c. The agreement of the model with the data shows the success of Regge phenomenology and indicates

TABLE IX. Density-matrix elements for the K^{*+}(890).

$-t$ range (GeV^2)	Events	Gottfried-Jackson frame ρ_{00}	ρ_{1-1}	Reρ_{10}	Helicity frame ρ_{00}	ρ_{1-1}	Reρ_{10}
0.00–0.05	186	0.458 ± 0.059	0.042 ± 0.045	−0.155 ± 0.031	0.615 ± 0.056	0.121 ± 0.041	−0.022 ± 0.035
0.05–0.10	272	0.350 ± 0.045	0.193 ± 0.038	−0.115 ± 0.025	0.416 ± 0.047	0.226 ± 0.035	0.073 ± 0.025
0.10–0.15	296	0.223 ± 0.041	0.253 ± 0.036	−0.099 ± 0.022	0.299 ± 0.043	0.291 ± 0.034	0.073 ± 0.022
0.15–0.20	296	0.186 ± 0.040	0.271 ± 0.035	−0.045 ± 0.022	0.197 ± 0.041	0.277 ± 0.036	0.036 ± 0.020
0.20–0.25	234	0.084 ± 0.040	0.218 ± 0.041	−0.073 ± 0.025	0.296 ± 0.048	0.324 ± 0.036	0.017 ± 0.023
0.25–0.30	182	0.108 ± 0.047	0.348 ± 0.044	−0.049 ± 0.027	0.132 ± 0.047	0.360 ± 0.044	0.047 ± 0.026
0.30–0.35	157	0.119 ± 0.049	0.302 ± 0.050	−0.015 ± 0.029	0.165 ± 0.053	0.325 ± 0.047	0.014 ± 0.029
0.35–0.40	125	0.083 ± 0.055	0.314 ± 0.057	0.031 ± 0.032	0.133 ± 0.060	0.339 ± 0.055	−0.036 ± 0.031
0.40–0.45	114	0.089 ± 0.058	0.221 ± 0.061	−0.072 ± 0.034	0.248 ± 0.067	0.301 ± 0.055	0.064 ± 0.034
0.45–0.50	79	0.068 ± 0.069	0.338 ± 0.072	−0.091 ± 0.039	0.120 ± 0.073	0.364 ± 0.069	0.094 ± 0.039
0.50–0.60	122	0.122 ± 0.058	0.413 ± 0.052	−0.034 ± 0.028	0.030 ± 0.055	0.368 ± 0.054	0.037 ± 0.029
0.60–0.70	79	0.049 ± 0.082	0.286 ± 0.093	0.073 ± 0.054	0.147 ± 0.072	0.335 ± 0.067	0.084 ± 0.043
0.70–0.80	41	0.144 ± 0.099	0.228 ± 0.094	−0.058 ± 0.059	0.175 ± 0.101	0.243 ± 0.095	0.056 ± 0.058
0.80–1.00	51	0.059 ± 0.086	0.311 ± 0.085	−0.011 ± 0.050	0.158 ± 0.085	0.360 ± 0.085	0.029 ± 0.051
All t	2341	0.192 ± 0.014	0.251 ± 0.013	−0.070 ± 0.008	0.257 ± 0.015	0.284 ± 0.012	0.036 ± 0.008

that A_2 exchange, as well as ρ exchange, is important in reaction (3).

B. The $K^{*+}(890)p$ Final State

In our study of the $K^{*+}(890)p$ final state, reaction (4), we have combined the data from reactions (2a), (2b), and (2b′). The $K^{*+}(890)$ is defined as a $(K\pi)^+$ mass combination in the interval $0.835 \leq M_{K\pi} \leq 0.955$ GeV.

The normalized decay distribution of a 1^- meson decaying into two pseudoscalar mesons is given by

$$W(\theta, \phi) = \frac{3}{4\pi}\left[\tfrac{1}{2}(1-\rho_{00}) + \tfrac{1}{2}(3\rho_{00}-1)\cos^2\theta - \rho_{1\,-1}\sin^2\theta\cos 2\phi - \sqrt{2}\ \mathrm{Re}\rho_{10}\sin 2\theta\cos\phi\right].$$

In Fig. 16 we show distributions of $\cos\theta$ and ϕ integrated over all other variables. From the $\sin^2\phi$ behavior of the Treiman-Yang angle, the ϕ distribution, it is clear that vector-meson exchange, natural parity, is important for $K^{*+}(890)$ produced in reaction (4).

In Fig. 17 we show the density-matrix elements in the Gottfried-Jackson frame as a function of t. The behavior of the density-matrix elements, elements at low t (large ρ_{00} and small $\rho_{1\,-1}$), indicates that pion exchange, unnatural parity, also contributes in reaction (4). In Table IX we tabulate the density-matrix elements in both the Gottfried-Jackson and the helicity frames.

Within the context of the absorptive model, we have attempted to account for reaction (4) using π and ω exchange. The results of this calculation are shown as the dashed curves in Fig. 17 and in Fig. 18, where we plot the differential cross section $d\sigma/dt$. The differential cross section is also tabulated in Table X.

The parameters used in our calculation of the absorptive model are

$$\gamma_i = 0.0707\,, \quad C_i = 0.873\,, \quad \gamma_f = 0.035\,, \quad C_f = 1.0\,,$$

with coupling constants of

$$(g_{K\pi K^*}G_{p\pi p/4\pi})^2 = 10.95\,,$$

$$[f_{K\omega K^*}(G^V_{p\omega p} + G^T_{p\omega p})/4\pi] = 3.63\,,$$

$$\frac{2G^T}{G^T + G^V} = 0.67\,.$$

Although the absorptive model gives good agreement with the density-matrix elements as a function of t, the agreement of the model with the scale and with the shape of the production distribution, Fig. 18, is poor.

Regge models again give good agreement with the data. We have explicitly calculated a Regge model proposed by Dass and Froggatt.[16-18] Our calculation of the model is shown as the solid curves in Figs. 17 and 18.

In reaction (4) both isovector and isoscalar exchanges are allowed. The residue functions for the isovector part of the exchange, the π and the A_2 trajectories, are determined by a fit to the charge-exchange reaction $K^-p \rightarrow K^{*0}(890)n$ which has no isoscalar exchanges. The isoscalar-exchange contribution, in the model we have calculated, is parametrized by an effective vacuum trajectory. The four parameters associated with this exchange were determined by a fit to the data of reaction (4) in a beam-momentum interval of 2–13

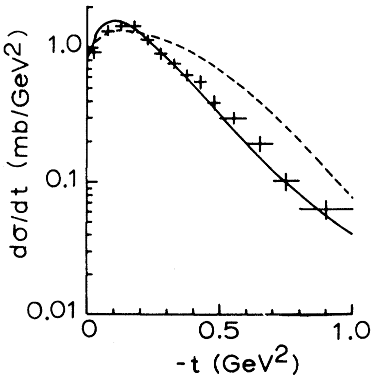

FIG. 18. Differential cross section $d\sigma/dt$ for the $K^{*+}(890)$. The curves result from the same models as in Fig. 17.

TABLE X. Differential cross section for the reaction $K^+p \rightarrow K^{*+}(890)p$.

$-t$ range (GeV^2)	Events	Cross section ($\mu\mathrm{b/GeV}^2$)
0.00–0.05	186	917 ± 80
0.05–0.10	272	1341 ± 104
0.10–0.15	296	1459 ± 110
0.15–0.20	296	1459 ± 110
0.20–0.25	234	1154 ± 94
0.25–0.30	182	897 ± 79
0.30–0.35	157	774 ± 72
0.35–0.40	125	616 ± 63
0.40–0.45	114	562 ± 59
0.45–0.50	79	389 ± 48
0.5–0.6	122	301 ± 31
0.6–0.7	79	195 ± 24
0.7–0.8	41	101 ± 17
0.8–1.0	51	63 ± 9
1.0–1.5	44	22 ± 4

GeV/c. Other parametrizations of the isoscalar-exchange contribution, which include both ω and P' exchange, give results qualitatively similar to the solid curves in Figs. 17 and 18.

As has been mentioned earlier, ρ_{00}, in some sense, measures the unnatural-parity $[P=(-1)^{J+1}]$ exchange for the $K^{*+}(890)$ produced in the helicity-0 state. In an analogous fashion, the linear combination of density-matrix elements

$$2\sigma^+ = \rho_{11} + \rho_{1\,-1}\,,$$
$$2\sigma^- = \rho_{11} - \rho_{1\,-1}$$

measures the amount of natural-parity exchange $[P=(-1)^J]$ and unnatural-parity exchange, respectively, for the $K^{*+}(890)$ produced in the helicity-1 state.[19]

In Fig. 19 we show $2\sigma^+$ and $2\sigma^-$, evaluated in the helicity frame, as a function of t. From these plots it is clear that there is little unnatural-parity exchange for $K^{*+}(890)$ produced in the helicity-1 state ($2\sigma^-$ is small for all t). The natural-parity contribution, measured by $2\sigma^+$, rises with t and levels off to a value of ~0.8, indicating that $K^{*+}(890)$ produced in the helicity-1 state is dominated by natural-parity exchange. In Fig. 20 we plot $(\rho_{00}+\rho_{11}-\rho_{1\,-1})d\sigma/dt$ and $(\rho_{11}+\rho_{1\,-1})d\sigma/dt$, which are respectively the differential cross sections for the unnatural-parity- and for the natural-parity-exchange contribution to $K^{*+}(890)$ production in reaction (4). The unnatural-parity-exchange cross section, dominated by pion exchange, shows no turnover in the forward direction. The natural-parity-exchange cross section shows a turnover in the forward direction indicative, as is the Treiman-Yang angular distribution, of vector-meson exchange.

C. The $K^{*+}(1420)p$ Final State

In our discussion of the $K^{*+}(890)$ and the $\Delta^{++}(1236)$, we have ignored the presence of a small nonresonant background beneath the resonance peaks. The background beneath the $K^{*+}(1420)$ is considerably larger and hence must be properly dealt with.

We define the $K^{*+}(1420)$ as a $(K\pi)^+$ mass combination in the mass interval $1.31 \leq M_{K\pi} \leq 1.51$ GeV. The principal source of background in this mass region is due to the crossing of the $K^{*+}(1420)$ band with the $\Delta^{++}(1236)$ band on the Dalitz plot. In order to remove this source of background, we first find the smallest interval of decay cosine in the $K\pi$ rest frame that contains all of the events in the $\Delta(1236)$ band $(0.8<\cos\theta_H<1.0)$. All of the events in this interval of $\cos\theta$ are then eliminated regardless of their πp mass. In order to correct for the events removed, we assume that the remaining events are in a predominant J^P state and are thus symmetric about a decay cosine of 0. We then repopulate with events from the angular region conjugate to the one eliminated. This procedure reduces the background level beneath the $K^*(1420)$, although a sizable background still remains. At our level of statistics we are unable to make further reliable background subtractions.

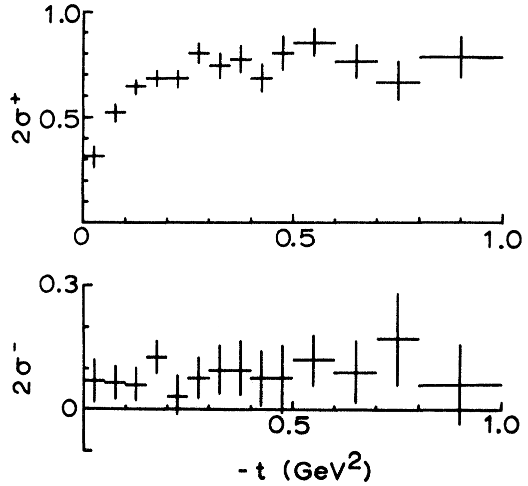

FIG. 19. $2\sigma^+$ and $2\sigma^-$ evaluated in the helicity frame as a function of t for the $K^{*+}(890)$.

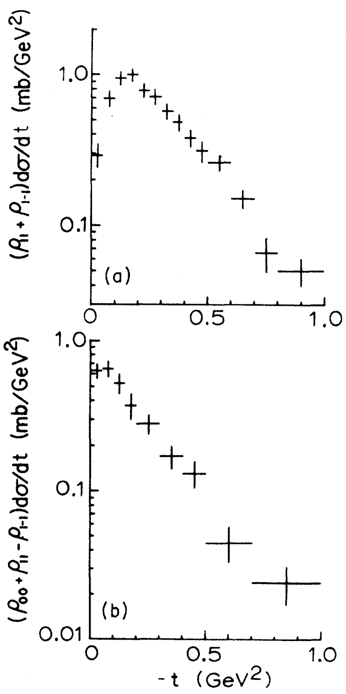

FIG. 20. Differential cross sections evaluated in the helicity frame for the $K^{*+}(890)$: (a) $(\rho_{11}+\rho_{1-1})d\sigma/dt$, (b) $(\rho_{00}+\rho_{11}-\rho_{1-1})d\sigma/dt$.

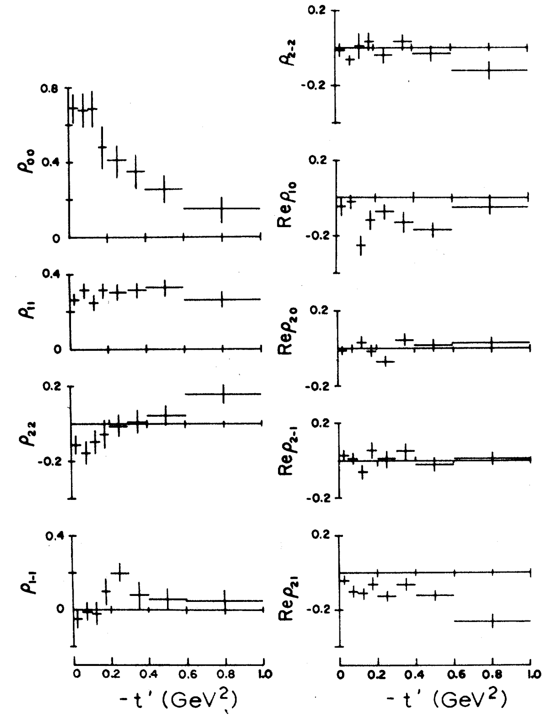

FIG. 21. Density-matrix elements in the Gottfried-Jackson frame as a function of t for the $K^{*+}(1420)$.

In Fig. 21 we plot the density-matrix elements, assuming $J^P = 2^+$, in the Gottfried-Jackson frame for the events remaining in the $K^*(1420)$ band as a function of $t' = |t - t_{\min}|$. As has already been noted elsewhere[5,20] ρ_{22} for $t' < 0.1$ is approximately 2 standard deviations negative. The most reasonable explanation of the nonphysical value of ρ_{22} is that it is due to interference between the dominant $2^+K\pi$ state and a 0^+ background. Due to the nonphysical value of ρ_{22}, the meaning of the other density-matrix elements is somewhat obscured. However, the large value of ρ_{00} is indicative of a sizable pion-exchange contribution to $K^*(1420)$ production in this reaction. For pure pion exchange, $\rho_{00} = 1$ and all other density-matrix elements are 0.

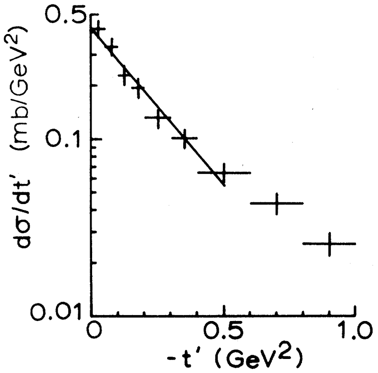

FIG. 22. Differential cross section $d\sigma/dt'$ for the $K^{*+}(1420)$. The curve is a fit to $d\sigma/dt' = A\ \exp(-Bt')$ in the t' range 0.0 to -0.5 GeV^2.

We also observe a sizable value for ρ_{11} and a nonzero value of $\rho_{1\,-1}$. Both of these are indicative of vector-meson exchange which predicts, in the absence of other processes, $\rho_{11} = 0.5$ and $\rho_{1\,-1} = 0.5$, with all other density-matrix elements equal to 0.

In Fig. 22 we plot the differential cross section, $d\sigma/dt'$. In this reaction, as opposed to $K^*(890)$ production, we observe no turnover in the forward direction. We have fitted the differential cross section in the range $0 < t' < 0.5$ to the form

$$\frac{d\sigma}{dt'} = A\ \exp(-Bt')$$

and find the parameters equal to

$A = 457 \pm 33\ \mu\text{b/GeV}^2$,

$B = 3.93 \pm 0.28\ \text{GeV}^{-2}$.

TABLE XI. Cross sections and resonance parameters averaged over all single-pion event types.

Reaction	Mass (MeV)	Width (MeV)	Cross section (mb)
$K^+p \to K^+p$	...	...	4.128 ± 0.122
$K^+p \to K^+p\pi^0$	...	...	0.404 ± 0.026
$K^+p \to K^0p\pi^+$	...	...	1.071 ± 0.035
$K^+p \to K^+n\pi^+$	...	...	0.679 ± 0.034
$K^{*+}(890) \to (K\pi)^+$	894.4 ± 0.8	60.7 ± 1.9	0.577 ± 0.029
$K^{*+}(1420) \to (K\pi)^+$	1409.3 ± 4.4	99.3 ± 15	0.128 ± 0.010
$\Delta^{++}(1236) \to p\pi^+$	1221.0 ± 1.3	90.1 ± 3.5	0.374 ± 0.018
$\Delta^+(1236) \to p\pi^0$	1219.9 ± 5.9	100.0 (input)	0.052 ± 0.006

VII. CONCLUSION

We have measured the elastic cross section, single-pion production cross sections, and resonance production cross sections as observed in K^+p interactions at 4.27 GeV/c. Cross sections and resonance parameters are collected in Table XI, where, for K^0 production, we have taken the weighted average between K^0 observed to decay in the bubble chamber and missing K^0.

In the $\Delta(1236)$ and $K^*(890)$ production distributions, we observed pronounced dips in the forward direction. These production distributions, as well as the resonance-decay distributions, are well accounted for by the Regge models discussed in the text.

ACKNOWLEDGMENTS

The author wishes to thank all the members of the University of Chicago Bubble Chamber group. Special thanks are due to Dr. B. Forman-Lasinski, Dr. T. Lasinski, and Dr. H. Schulz. Most of all, I wish to thank Dr. N. Gelfand, whose advice, encouragement, and support have proved invaluable for the length of this work.

---

*This work was supported in part by the National Science Foundation under Grant No. GP 29663.

†Presented as a thesis to the Department of Physics, the University of Chicago, in partial fulfillment of the requirements for the Ph.D. degree.

‡E. F. I. research assistant, 1966–69 and 1970–72. E. I. DuPont Fellow, 1969–70.

§Present address: Harrison M. Randall Laboratory, University of Michigan, Ann Arbor, Mich. 48103.

[1] W. De Baere *et al.*, Nuovo Cimento 51A, 401 (1967).

[2] C. Fu, J. MacNaughton, and G. H. Trilling, Nucl. Phys. B28, 528 (1971).

[3] E. Flaminio, J. D. Hansen, D. R. O. Morrison, and H. Tavey, CERN Report No. CERN/HERA 70-4 (unpublished).

[4] L. Price *et al.*, LRL Report No. UCRL-20000 K^+N (unpublished).

[5] M. Aguilar-Benitez, R. L. Eisner, and J. B. Kinson, Phys. Rev. D 4, 2593 (1971).

[6] R. J. Plano and D. H. Tycko, Nucl. Instr. Methods 20, 458 (1963).

[7] R. Bock, CERN Report No. CERN 61-29, 1961 (unpublished).

[8] There were 83 events which satisfied the criteria in two ways. Choosing the hypothesis with the lower χ^2 does not influence any of our conclusions.

[9] A similar analysis is used in Ref. 1.

[10] Using the quadratic extrapolation, we find $\omega^2 = 0.098 \pm 0.029$.

[11] M. Davier and H. Harari, Phys. Letters 35B, 239 (1971).

[12] J. D. Jackson, Nuovo Cimento 34, 1644 (1964).

[13] L. Stodolsky and J. J. Sakurai, Phys. Rev. Letters 11, 90 (1963).

[14] J. T. Donahue, Phys. Rev. 163, 1549 (1967).

[15] M. Krammer and U. Maor, Nuovo Cimento 52A, 308 (1967).

[16] G. V. Dass and C. D. Froggatt, Nucl. Phys. B8, 661 (1968).

[17] G. V. Dass and C. D. Froggatt, Nucl. Phys. B10, 151 (1969).

[18] G. V. Dass and C. D. Froggatt, Nucl. Phys. B19, 611 (1970).

[19] J. P. Ader and M. Capdeville, Nuovo Cimento 56A, 952 (1968).

[20] R. Engelmann *et al.*, Phys. Rev. D 5, 2162 (1972).